# Investigation on the demetallation of Fe-N-C for oxygen reduction reaction: The influence of structure and structural evolution of active site

Xinlong Xu [a,b,1], Xiaoming Zhang [a,b,1], Zhichong Kuang [c], Zhangxun Xia [a,b], Alexandre I. Rykov [c], Shansheng Yu [d], Junhu Wang [c,*], Suli Wang [a,b,**], Gongquan Sun [a,b,**]

[a] Division of Fuel Cells and Battery, Dalian National Laboratory for Clean Energy, Dalian Institute of Chemical Physics, Chinese Academy of Sciences, Dalian 116023, PR China
[b] Key Laboratory of Fuel Cell & Hybrid Power Sources, Dalian Institute of Chemical Physics, Chinese Academy of Sciences, Dalian 116023, PR China
[c] Mössbauer Effect Data Centre, Dalian Institute of Chemical Physics, Chinese Academy of Sciences, Dalian 116023, PR China
[d] Department of Materials Science, Jilin University, Changchun 130012, PR China

ABSTRACT

Iron-nitrogen-carbon (Fe-N-C) catalysts for oxygen reduction reaction (ORR) are promising candidates in fuel cell devices but the poor stability remains a grave challenge. The elimination of demetallation is pivotal for extending the life but still incapable due to the ambiguous mechanism. Herein, we show that the structure of $FeN_4$ site and its structural evolution during ORR has the significant influence. The end-of-test/in-situ Mössbauer spectroscopy and density functional theory study reveal that D1 mainly contributes to the ORR activity but suffers severe demetallation, which is likely due to the instability of $FeN_4C_8$. The faster demetallation during ORR, especially at higher potential, can be attributed to the weaker coordination of $FeN_4$ induced by oxygenated intermediate and electric field according to ab initio molecular dynamics simulations. Finally, the binding energy of Fe-N bond is introduced to describe the influence of structure and structural evolution and give guidance to the improvement of stability.

## 1. Introduction

Polymer electrolyte membrane fuel cells (PEMFCs), featured with clean and high energy conversion efficiency, have emerged as the promising electricity-generating technology for automobile propulsion and power station [1,2]. But the commercialization is severely hindered by the high cost and scarcity of Pt-based catalysts, and the heavy use of Pt in the cathode due to the sluggish oxygen reduction reaction (ORR) is the main contradiction [3]. In the last decades, tremendous efforts have been devoted to the exploration of non-precious metal catalysts (NPMCs) on ORR [4–6], and the rapid escalation on the activity of iron-nitrogen-carbon (Fe-N-C) catalysts brings lights on low-cost PEMFC devices [7,8]. However, except for some remarkable works [9,10], poor stability is commonly observed in most PEMFCs assembled with Fe-N-C, making it strenuous to meet the requirement of practical application [11]. Therefore, the stability issue becomes one of the most critical challenges for Fe-N-C catalysts.

The degradation of Fe-N-C may origin from reduced active site density (SD), turnover frequency (TOF) and limited mass transport, thus deducing a series of possible mechanisms including demetallation, protonation of nitrogen groups followed by anion adsorption, carbon corrosion and mild surface oxidation by hydroxyl free radicals (·OH) [12–16]. In recent progress, numerous experimental and theoretical results reveal the high ORR activity of the coordinated structure of Fe and N ($FeN_x$) [17–19]. Therefore, many researchers blame the degradation of Fe-N-C on the destruction of $FeN_x$, especially on the dissolution of central Fe atoms from $FeN_x$ known as demetallation [20,21]. According to the Pourbaix diagram developed by Zelenay et. al., demetallation is thermodynamically favored under PEMFC-relevant acidic environments [22]. Experimentally, demetallation is identified by a series of in-situ and operando characterizations. The clear evidence of the irreversible demetallation of iron(II) phthalocyanine (FePc) in the

---

* Corresponding author.
** Corresponding authors at: Division of Fuel Cells and Battery, Dalian National Laboratory for Clean Energy, Dalian Institute of Chemical Physics, Chinese Academy of Sciences, Dalian 116023, PR China.
*E-mail addresses:* wangjh@dicp.ac.cn (J. Wang), suliwang@dicp.ac.cn (S. Wang), gqsun@dicp.ac.cn (G. Sun).
[1] These authors contributed equally to this work.

acidic medium is found by electrochemical tip-enhanced Raman spectroscopy (EC-TERS) [23]. The transformation from active FeN$_4$ to inactive ferric oxides is also demonstrated by $^{57}$Fe Mössbauer spectroscopy [14]. These results confirm that demetallation is dominantly responsible for the degradation of Fe-N-C.

On this account, to improve the stability of Fe-N-C, one of the centerpieces is to slow down the rate of demetallation. However, the mechanism of demetallation remains unrecognizable so far, because complex contributing factors are involved in the process. First, the structure of active site has a significant influence as the chemical stability is quite sensitive to the molecular structure [14,21,24,25]. Furthermore, the rate of demetallation is varied with conditions including different pH, potential and temperature etc. [12,13,26–28]. Especially, these structural and conditional factors are intertwined, e.g., the structure of active site is heavily dependent on the operating condition and medium, raising the challenge for the interpretation of the inner relationship [29,30]. Therefore, to get insight into the mechanism of demetallation, the analysis of the fine structure of FeN$_x$ at the molecular level is indispensable, especially for the in-situ observation of the dynamic transition under the working condition.

Herein, the degradation of Fe-N-C induced by demetallation is confirmed by correlating the dissolution of Fe to the performance loss using electrochemical and physical methods. Then the mechanism of demetallation is investigated by bridging the experimental and theoretical studies. The activity and stability of different types of FeN$_4$ are distinguished by EoT and in-situ $^{57}$Fe Mössbauer spectroscopy and further confirmed by DFT calculations. The stability of Fe-N-C under different conditions is evaluated and the influence of structural evolution on demetallation during ORR is investigated using ab initio molecular dynamics (AIMD) simulations. The binding energy of Fe-N bond is introduced as the descriptor for the influence of structure and structure evolution. On this basis, some promising active sites with high stability are estimated and the rational optimization of operating conditions is also proposed for relieving demetallation and improving the stability.

## 2. Experimental

### 2.1. Synthesis of Fe-N-C

For preparing Fe-N-C, 1782 mg 2-methylimidazole, 814 mg ZnO, 26 mg iron(II) acetate, 520 mg phenanthroline and 7 g agate ball (d=6 mm) were sealed in a jar and balled-mill for 3 h under N$_2$ protection. Then the mixture was dealt with microwave (900 W, 2450 MHz) for 15 min to form ZIF-8. The obtained precursor was annealed at 1050ºC for 1 h under N$_2$ with a flow of 400 mL min$^{-1}$. After washed with 0.1 M HCl, the catalyst suffered secondary heat treatment at 900ºC for 15 min under NH$_3$ with a flow of 30 mL min$^{-1}$ (the atmosphere was switched to N$_2$ during ramping and cooling) to obtain Fe-N-C for stability study.

For preparing $^{57}$Fe-N-C, 15.8 mg $^{57}$Fe was dissolved by a few drops of 0.1 M HCl and then 15 mL H$_2$O was added to dilute the solution. 982 mg phenanthroline was added in the solution and stirred for 8 h. Then the solvent was vapored away. The obtained solid was mixed with 3.36 g 2-methylimidazole and 1.54 g ZnO to suffer ball-milling. The ball-milling and subsequent pyrolysis procedure are the same as that for preparing Fe-N-C. Finally, $^{57}$Fe-N-C is obtained for Mössbauer spectroscopy study.

### 2.2. Physical characterizations

X-Ray diffraction (XRD) was conducted on Rigaku D/Max-2500 with Cu Kα radiation. Transmission electron microscope (TEM) was conducted on JEM-2100 F microscope. N$_2$ adsorption isotherm was conducted on Quantachrome NOVA 2200e at 77.4 K. For X-ray photoelectron spectroscopy (XPS) tests, several drops of the ink for electrochemical tests were dropped on a piece of indium foil and dried, which was used for determining the state of Fe-N-C at initial. After the

aging test, the Fe-N-C on the electrode was dispersed in ethanol by ultrasound and washed for several times. Then the sample was also dropped on a piece of indium foil and dried, which was used for determining the state of Fe-N-C after degradation. XPS of the two sample was conducted on Thermo ESCALAB 250. The Fe content in the electrolyte was determined by inductively coupled plasma mass spectrum (ICP-MS) using NexION 300D.

### 2.3. Electrochemical measurements

The electrochemical measurements were conducted in 0.1 M HClO$_4$ with a volume of 160 mL at 30ºC using CHI 760e electrochemical workstation. The counter and reference electrode are graphitic rod and saturated calomel electrode (SCE), respectively. The reference electrode was experimentally calibrated by a reversible hydrogen electrode (RHE). Fe-N-C was coated on the glassy carbon disk of rotating disk electrode (RDE) with a loading of 0.8 mg cm$^{-2}$ as the working electrode using Nafion as the binder. The aging test was conducted by chronoamperometry at different potentials. After each segment of 10 h, the cyclic voltammetry (CV) curve was collected in the N$_2$-saturated electrolyte with a scan rate of 10 mV s$^{-1}$, the linear sweep voltammetry (LSV) curve was collected in the O$_2$-saturated fresh electrolyte with a scan rate of 10 mV s$^{-1}$ and a rotating speed of 1600 rpm.

### 2.4. End of state and in-situ Mössbauer spectroscopy

For end of state (EoT) Mössbauer spectroscopy tests, $^{57}$Fe-N-C was sprayed on the rectangle carbon paper (1.5 *8 cm$^2$) with an active area of 1 cm$^2$ and loading of 4 mg cm$^{-2}$ (0.5 wt% Nafion). Five pieces of the carbon paper was assembled into a multilayer electrode and a space of 1 mm is exiting between each layer. The electrode was immersed in O$_2$-saturated 0.1 M HClO$_4$ to suffer aging tests at different potential (0.3, 0.5 and 0.7 V) for 150 h. Then the electrode was washed by DI water for several times and dried. The Mössbauer spectra was collected at the ambient environment using $^{57}$Co radioactive source and Topologic 500 A spectrometer. For in-situ Mössbauer spectroscopy tests, the $^{57}$Fe-N-C electrode was immersed in the designed electrochemical cell purged with O$_2$ with the graphitic rod and Ag/AgCl electrode as the counter and reference electrode. The spectra were collected for 24 h under OCP and different potential (0.3, 0.5 and 0.7 V).

### 2.5. Theoretical simulations

All DFT calculations were conducted with the Dmol$^3$ program package [31,32]. The detail calculation parameters could be found in our previous work [33]. In the ab initio molecular dynamics (AIMD) simulations, the aqueous solution is simulated using conductor-like screening model (COSMO) and the dielectric constant is set as 78.54. First-principles molecular dynamics (MD) was performed with NVE method. A time step of 1 fs was used and the temperature was set to 298.15 K. In this work, a local electric field has been applied to simulate the electrical double layer (EDL). For PEMFCs, the thickness of the EDL associated with an H$_2$O solvent is about 3 Å, thus the three-phase interface of the cathode may experience a local electric field on the order of $10^9$ V m$^{-1}$ [34]. In this work, the binding energy is calculated as:

$$E_b = E_{Fe-N-C} - E_{N-C} - E_{Fe}$$

The formation energy is defined by:

$$E_f = E_{Fe-N-C} - x\mu_C - y\mu_N - \mu_{Fe}$$

$E_{Fe-N-C}$ is the total energy of the Fe-N-C slab, $E_{N-C}$ is the energy of Fe-N-C slab with removed Fe atom, $E_{Fe}$ is the energy of an isolated Fe atom, and $\mu_C$, $\mu_N$ and $\mu_{Fe}$ are chemical potentials of carbon (graphite), nitrogen (N$_2$) and iron (bulk Fe), respectively.

## 3. Results and discussion

### 3.1. Synthesis and characterization of Fe-N-C

A model Fe-N-C catalyst was prepared using iron acetate, 1,10-phenanthroline and zeolitic imidazolate framework (ZIF) as the precursor according to the literature [35]. TEM, XRD and $N_2$ isothermal sorption curve of as-prepared Fe-N-C are presented in Figs. S1–3. In brief, the Fe-N-C catalyst is composed with highly graphitized porous carbon matrix and uniformly dispersed Fe and N, which forms into $FeN_4$ as revealed by Mössbauer spectroscopy in the later part.

### 3.2. Demetallation during the degradation of Fe-N-C

A five segments degradation test for 10 h each was performed at a constant potential of 0.7 V versus reversible hydrogen electrode (vs. RHE) in $O_2$-saturated 0.1 M $HClO_4$, and the relevant electrochemical measurements and physical characterizations after each segment were conducted as labeled in Fig. 1a. It's observed that the ORR current decreases sharply in the first 10 h, then mildly with a similar rate in the next 40 h, and finally retains only 34.7% after 50 h. The corresponding LSV curves also confirm a fast decay at initial and slow decay afterward (Fig. S4 and Table S1). The non-uniform rate is strongly related to the demetallation of different types of $FeN_4$ as revealed in the following section.

The CV curve of the pristine Fe-N-C is approximately quadrilateral, mostly attributed to the double layer capacitance of the porous carbon matrix. But two pairs of redox peaks are observed to intensify as the elapsed time at the range of 0.5–0.6 V and 0.7–0.8 V, respectively (Fig. 1b). The peaks at 0.5–0.6 V are related to the redox of pyrrolic-N and pyridinic-N involving protons in the acidic medium ($N_{proton}$) [36, 37]. In Fig. S5, the deconvoluted N1s XPS of the pristine Fe-N-C exhibit five characteristic peaks: pyridinic-N (~398.2 eV), Fe-N (~399.3 eV),

pyrrolic-N (~400.3 eV), graphitic-N (~401.1 eV) and oxidized-N (~402.4 eV). After degradation, an obvious protonation-N peak appears at 401.6 eV with a ratio of 15.04% [38]. Correspondingly, the content of pyridinic-N and Fe-N decreases, indicating the crack of Fe-N coordination and the protonation of nitrogen [39]. According to the Pourbaix diagram [30,40], the peaks at 0.7–0.8 V are attributed to the redox of $Fe^{2+}/Fe^{3+}$ ($Fe_{redox}$), which may originate from the Fe in both Fe-N-C and electrolyte. Herein, the contribution of soluble Fe to $Fe_{redox}$ peaks is confirmed as follow: (1) $Fe_{redox}$ peaks are inconspicuous in the CV curve of pristine Fe-N-C; (2) $Fe_{redox}$ peaks disappear once the original electrolyte after aging is substituted by a fresh one (Fig. 1c); (3) ICP-MS confirms the increasing content of soluble Fe in the electrolyte along with the aging test (Fig. 1d). Moreover, the dissolved Fe content increases sharply with a rate of 0.193 ppb $h^{-1}$ in the first 10 h but slowly with a rate of 0.076 ppb $h^{-1}$ in the subsequent 40 h, which shows consistency to the degradation rate and confirms the correlation between the demetallation and degradation of Fe-N-C. Notably, the dissolved Fe cations are usually observed as the degradation product when performing the aging test on RDE but they precipitated into Fe oxide at 80 °C in PEMFCs [12]. Furthermore, the demetallation is also identified by the higher hydrophilicity of Fe-N-C after the aging test due to the exposure of N atoms with lone-pair N2p electrons after the disassociation of Fe, which may lead to water flooding of the cathode catalyst layer (CCL) (Fig. 1e) [37,41]. Besides, leached Fe ions are proved to enlarge the proton conduction resistance in membrane and CCL [42]. As illustrated in Fig. 1f, demetallation not only directly results in the reduced active site density, but is also the inducement of limited mass transport and proton conductivity. Therefore, the elimination of demetallation is pivotal for improving the stability of Fe-N-C.

### 3.3. Demetallation of different types of $FeN_4$

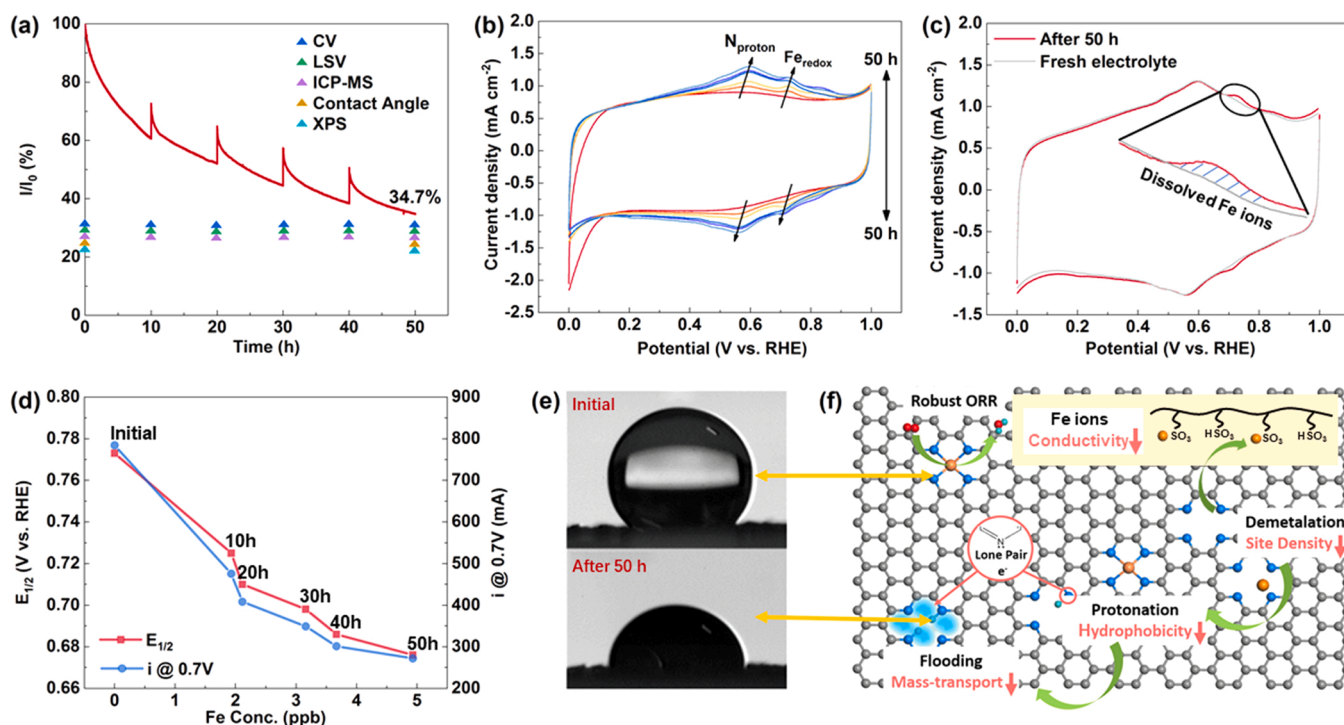Demetallation of $FeN_4$ with different structures is investigated using



**Fig. 1.** Demetallation during the degradation of Fe-N-C. (a) Normalized current density of Fe-N-C as a function of time, the electrode was polarized at a constant potential of 0.7 V vs. RHE for 50 h in $O_2$-saturated 0.1 M $HClO_4$, the triangle symbols represent the corresponding tests conducted at the time; (b) CV curves of Fe-N-C in the $N_2$-saturated electrolyte recorded at the beginning and after every 10 h; (c) CV curves of Fe-N-C after aging for 50 h in the original and fresh electrolyte; (d) The ORR performance of Fe-N-C as a function of the content of dissolved Fe determined by ICP-MS; (e) The contact angle of the Fe-N-C electrode at initial and after 50 h aging test; (f) The illustration of the degradation of Fe-N-C related to demetallation.

[57]Fe Mössbauer spectroscopy, which is extremely sensitive to the coordinate structure of Fe [43]. To acquire a high signal-to-noise ratio (SNR), the [57]Fe-N-C catalyst was synthesized by the same protocol using [57]Fe, which was highly consistent in structure and electrochemical performance with Fe-N-C (Figs. S6–8). First, EoT spectrums were collected for electrodes experienced the aging of 150 h under different potentials (0.3 V, 0.5 V and 0.7 V) (Fig. S9). The spectrum can be fitted into four doublets, labeled as D1, D2, D3 and D4 (Fig. 2a and Table S2). D1, D2 and D4 have the comparable IS in the range of 0.31–0.39 mm s$^{-1}$, while their QS are different in the range of ~1.3 mm s$^{-1}$, ~2.9 mm s$^{-1}$ and ~0.8 mm s$^{-1}$, respectively. D1 is most often assigned to low-spin FeN$_4$C$_8$ or high-spin FeN$_4$C$_{12}$ moieties, and considered with exceptionally high ORR activity [8,14]. D2 is commonly assigned to low- or intermediate-spin FeN$_4$C$_{10}$ moieties. The more inner doublet D4 with lower QS is recognized as FeN$_4$ adsorbed with oxygen species, which has been found in FePc treated by O$_2$ or Fe-N-C exposed to O$_2$ analogs [44,45], and also confirmed by the in-situ observation and DFT calculation in recent progress [14,46]. The exceptionally high IS and QS of D3 may origin from the additional coordination of FeN$_4$ site by two weak ligands (XY-FeN$_4$) or the fivefold-coordinated N-FeN$_{2+2}$...N$_{prot}$/C site. In this work, the former is more likely because N-FeN$_{2+2}$...N$_{prot}$/C is well-known for its fast deactivation while the content of D3 remains changeless after the aging test. But XY-FeN$_4$ is indicated to contribute less to ORR due to its saturated coordination that obstructs the interaction between the 3d orbital of the central Fe atom and the * π orbital of O$_2$ [47,48].

First, the degradation of Fe-N-C due to demetallation can be further verified by the EoT [57]Fe Mössbauer spectroscopy (Fig. 2a-b) and electrochemical measurements (Fig. S10), because the more significant demetallation of D1 and D2 is observed along with the faster decay at higher potential. Compared with the pristine Fe-N-C, the content of D1 and D2 decreases slight at 0.3 V and 0.5 V, but drops sharply at 0.7 V. Correspondingly, the loss of current density in the chronoamperometric curve and E$_{1/2}$ in the LSV curve is also more significant at 0.7 V. Moreover, the demetallation rate of D1 and D2 differs in degree. D1 suffers a loss from 44.99% to 37.85% after aging at 0.7 V, while the loss of D2 is from 29.74% to 25.29%. The faster loss of D1 than D2 strongly suggests the influence of structure on the demetallation of FeN$_4$ site.

To further reveal the influence of structure, in-situ Mössbauer spectroscopy of Fe-N-C at different potentials was conducted and the details for the fabrication of electrode and device are illustrated in Fig. S11. As shown in Fig. 2c, the decrease of D1 and D2 and the increase of D4 are observed, corresponding to the transformation from the bare FeN$_4$ to FeN$_4$ adsorbed with oxygen-containing intermediates in the typical ORR procedure [29]. At 0.7 V, a decrease of D1 from 49.09% to 35.04% and an increase of D4 from 18.88% to 32.06% is observed while the content of D2 is less changed. Under lower potential when the reaction is accelerated and more intermediates are involved, the more significant transition of D1 and the slight transition of D2 are observed (Fig. 2d and Table S3). It indicates D1 mainly contributes to the ORR activity while D2 only contributes under the high overpotential. Therefore, by combining the result of EoT and in-situ Mössbauer spectroscopy, it reveals that D1 and D2 suffers demetallation with different rates and the fast demetallation of D1 is truly responsible for the rapid degradation of Fe-N-C.

The demetallation related to the structure of FeN$_4$ is further demonstrated using DFT calculations. The IS and QS of D1 are well identical with FePc [44], and ever proposed to be a FeN$_4$C$_8$ structure consisting of a Fe-ion coordinated by four nitrogenous groups [8,47]. Recent progress suggests that a FeN$_4$C$_{12}$ structure also exists by bridging the DFT, Mössbauer spectroscopy and extended X-ray absorption fine structure (EXAFS) study [18,46]. The coexist of the two structures in D1 is reasonable as Fe-N-C is a complex mixture. D2 is generally assigned to FeN$_4$C$_{10}$ according to the literature (Fig. 3a) [8,14]. The Gibbs free energy of each step in the continuous 4e$^-$ ORR pathway on different types of FeN$_4$ are calculated (Figs. S12–14, Tables S4 and 5) and plotted in Fig. 3b. An energy barrier of 0.37 eV for the rate-determining step (RDS) is observed on FeN$_4$C$_{10}$, which is much higher than that of FeN$_4$C$_8$ and FeN$_4$C$_{12}$ (Fig. 3c). This is consistent with the in-situ Mössbauer spectroscopy results that D1 mainly contribute to the ORR activity. However, the strength of Fe-N bond in FeN$_4$C$_{12}$ is more robust than FeN$_4$C$_8$ for its lower binding energy (Fig. 3d and Table S6), indicating that FeN$_4$C$_8$ suffers a more intense demetallation. Considering that the binding energy of FeN$_4$C$_{12}$ is also lower than FeN$_4$C$_{10}$ while D2 (normally assigned to FeN$_4$C$_{10}$) only suffers a slight demetallation, it's inferred that FeN$_4$C$_{12}$ possesses both high activity and stability. Therefore, the fast decay of Fe-N-C in the early period can be related to the demetallation of unstable FeN$_4$C$_8$ while the remained activity with a low
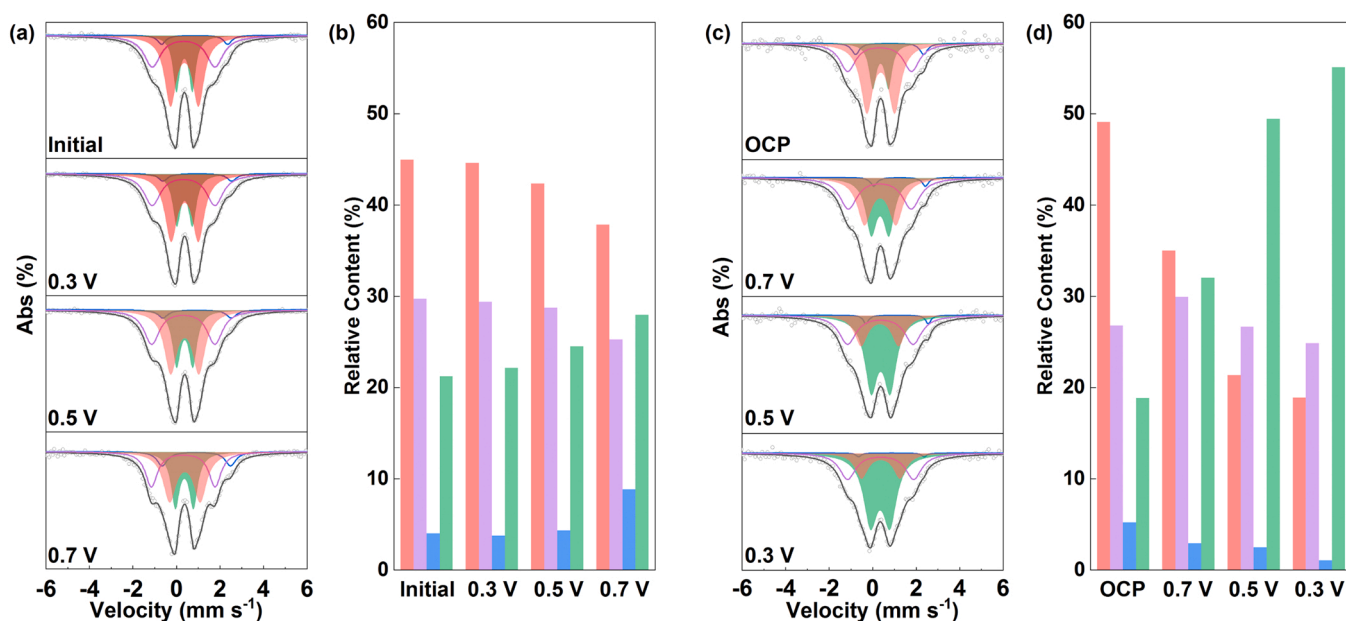


**Fig. 2.** EoT and in-situ [57]Fe Mössbauer spectroscopy on [57]Fe-N-C. (a) The EoT Mössbauer spectra of the [57]Fe-N-C at the initial state and after degradation at different potentials for 150 h and (b) the corresponding relative content of different types of FeN$_4$; (c) The in-situ Mössbauer spectra of the [57]Fe-N-C under different potentials and (d) the corresponding relative content of different types of FeN$_4$ (Red: D1; Purple: D2; Blue: D3; Green: D4).
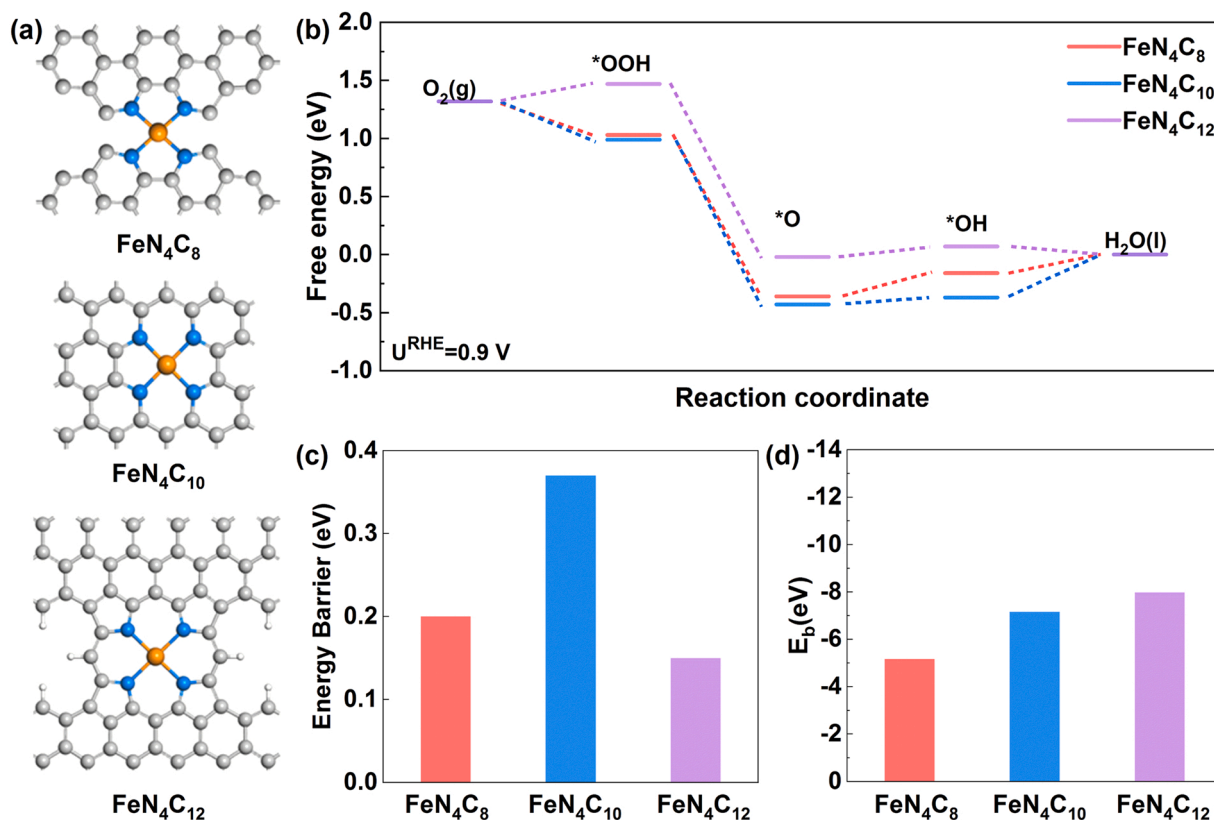
**Fig. 3.** DFT study on the activity and stability of various $FeN_4$. (a) The schematic structure of $FeN_4C_8$, $FeN_4C_{10}$ and $FeN_4C_{12}$; (b) The free energy diagram and (c) the energy barrier of the rate-determining step for ORR through a 4e⁻ pathway in the acidic medium on different $FeN_4$ sites; (d) The binding energy of Fe-N bond in different $FeN_4$ sites.
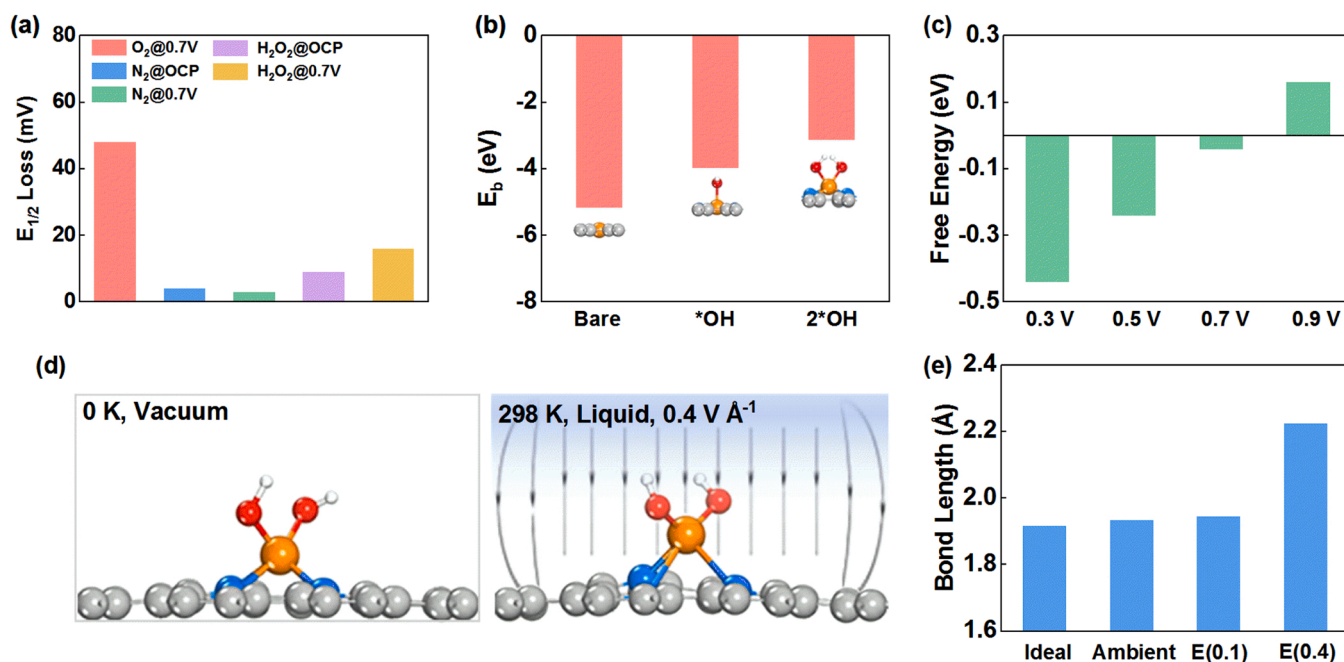


**Fig. 4.** Study on the influence of structural evolution. (a) The loss of $E_{1/2}$ after the first 10 h under different conditions; (b) The Fe-N binding energy of $FeN_4C_8$ adsorbed with different amounts of *OH; (c) the free energy for the desorption of *OH from $FeN_4C_8$ under different potentials; (d) The illustration of the AIMD simulations and (e) The average bond distance in $FeN_4C_8$ * 2OH under Ideal, Ambient and Electric field state. The Ideal state is defined as in the vacuum at 0 K; the Ambient state is defined as in the electrolyte at 298 K; the E(0.1) and E(0.4) states are defined as in the electrolyte at 298 K coupled with 0.1 V Å⁻¹ and 0.4 V Å⁻¹ electric field, respectively.

decay rate at the later stage can be attributed to $FeN_4C_{12}$, corresponding to the residual D1 in the Mössbauer spectra after degradation.

### 3.4. Demetallation induced by structural evolution during ORR

The structural evolution of $FeN_4$ sites under different conditions has been well investigated previously [40,49], but its influence on stability still remains exploration. According to a sequence of electrochemical experiments with controlled conditions (schemed in Fig. S15), Fe-N-C exhibits different degradation rates under different conditions. As shown in Fig. 4a, the $E_{1/2}$ is negatively shifted for 47 mV after 10 h under the operating condition of ORR (at 0.7 V in $O_2$-saturated 0.1 M $HClO_4$). However, when just immersing Fe-N-C in $N_2$-saturated 0.1 M $HClO_4$ or further applying a potential of 0.7 V (corresponding to ORR-free states), a negligible performance loss is observed (Fig. S16). According to the in-situ Mössbauer spectra (Fig. 2c), the transformation from bare $FeN_4$ to $FeN_4$ adsorbed by oxygenated intermediate is observed during ORR. By DFT calculations, it's revealed that the binding energy of Fe-N bond gets higher when adsorbed by oxygenated intermediate, corresponding to a weakened bond strength (Fig. 4b, Fig. S17 and Table S6). Therefore, the demetallation gets more severe when ORR occurs. The influence of oxygenated intermediates can be further identified by introducing $H_2O_2$ as the reactant because it's also involved in the electrochemical reduction on $FeN_4$, which results in oxygenated intermediates [50]. As shown in Fig. S18, when just immersing Fe-N-C at OCP in the electrolyte containing 0.1 wt% $H_2O_2$ for 10 h, the loss of $E_{1/2}$ is 9 mV, which could be attributed to the mild oxidation mechanism by hydroxyl radicals [12,13]. However, when applying a potential of 0.7 V, the loss of $E_{1/2}$ jumps to 16 mV and further increases along with the increased concentration of $H_2O_2$. The extra decay can be attributed to the accelerated demetallation through the formation of oxygenated intermediates on $FeN_4$ during $H_2O_2$ reduction according to above results.

The effect of potential on the structural evolution can be considered from two aspects. On the one hand, the adsorption behavior of oxygenated intermediate is heavily dependent on the potential. As revealed by DFT calculations (Fig. 4c, Fig. S19 and Table S7), the free energy for the desorption of oxygenated intermediate gets higher as the potential increases. It indicates a stronger adsorption which has also been identified by the increased coordination number of Fe in the in-situ EXAFS study previously [29,51]. As revealed in Fig. 4b and Fig. S17, along with the more adsorption of oxygenated intermediate, the Fe-N bond is further weakened. Therefore, the more severe demetallation and accelerated degradation of Fe-N-C are observed at higher potential [26,52]. On the other hand, the electric field in the double electric layer

has influence on the transition state of active site [53,54]. The ab initio molecular dynamics (AIMD) simulations, which imitate the realistic ORR state, are further conducted to study the structural evolution of active site under the ideal and electric field states (0.1 V $Å^{-1}$ and 0.4 V $Å^{-1}$) (Fig. 4d). As shown in **Movie 1–3**, when coupled with solvent and electric field under 298 K, $FeN_4$ with adsorbed oxygen species undergoes a more violent vibration along with the increase of field intensity (Fig. 4e and Table S8). At 0.4 V $Å^{-1}$, the Fe-N bond is stretched with a maximum distance of 2.730 Å, which 1.43 times longer than that of bare $FeN_4C_8$ (1.841 Å) and exceeds that in most general Fe compounds (Table S9). According to the empirical bond-strength-bond-length theory [55], the stretching of Fe-N bond to such a dramatical degree makes the bond strength less than 20% of the initial (Fig. S20). Therefore, the fast degradation of Fe-N-C during ORR, especially at higher potential, can be attributed to the structural evolution due to the adsorption of oxygenated intermediate and motivation of electric field.

Supplementary material related to this article can be found online at doi:10.1016/j.apcatb.2022.121290.

For better understanding, those structure and structural evolution factors are summarized by using the binding energy of Fe-N in the active site as the descriptor. As shown in Fig. 5a-b, under the ideal state, the active site with higher Fe-N binding energy in the initial structure, such as $FeN_4C_8$, suffers the more severe demetallation due to its weak coordination. During ORR when the site is adsorbed with oxygenated intermediate and located in the electric field, the binding energy further gets higher and leads to the sharp decrease of Fe-N bond strength and rapid demetallation. Therefore, the rational structural design of active sites and the tuning of reaction environments demands urgently for the improvement of stability.

### 3.5. Suggestions on the alleviation of demetallation

According to the above, active sites with both high activity and stability are fascinating for desired Fe-N-C catalysts. On this account, the activity and stability of a series of $FeN_4$ structures are investigated by using the binding energy as the stability descriptor and energy barrier of RDS as the activity descriptor, which can also be expanded into other metal (Mn, Fe, Co, Ni, Cu, Zn) and nitrogen coordinated structures (Figs. S21–25 and Table S10). As circled in Fig. 6, besides $FeN_4C_{12}$, porphyrin-like $FeN_4$ and phthalocyanine-like $FeN_4$, some other sites composed of Mn (phthalocyanine-like $MnN_4$ and $MnN_4C_{12}$) and Co ($CoN_4C_{10}$) also possess relatively high activity and stability. Those Fe-free sites exhibit lower formation energy than the akin Fe sites,
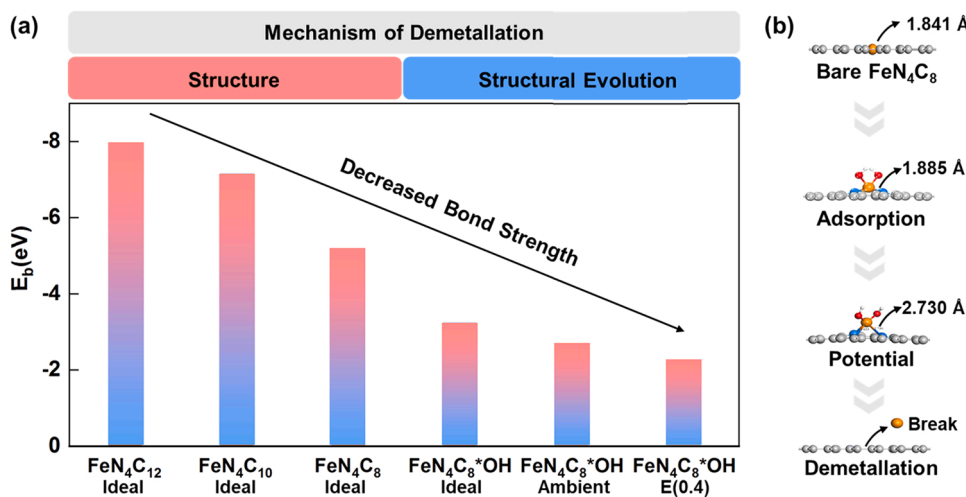


**Fig. 5.** The general description of the finding. (a) The influence of structure and structural evolution on demetallation using the binding energy of Fe-N bond as the descriptor; (b) The illustration of the bond-breaking process due to the increased bond distance and decreased bond strength of Fe-N.
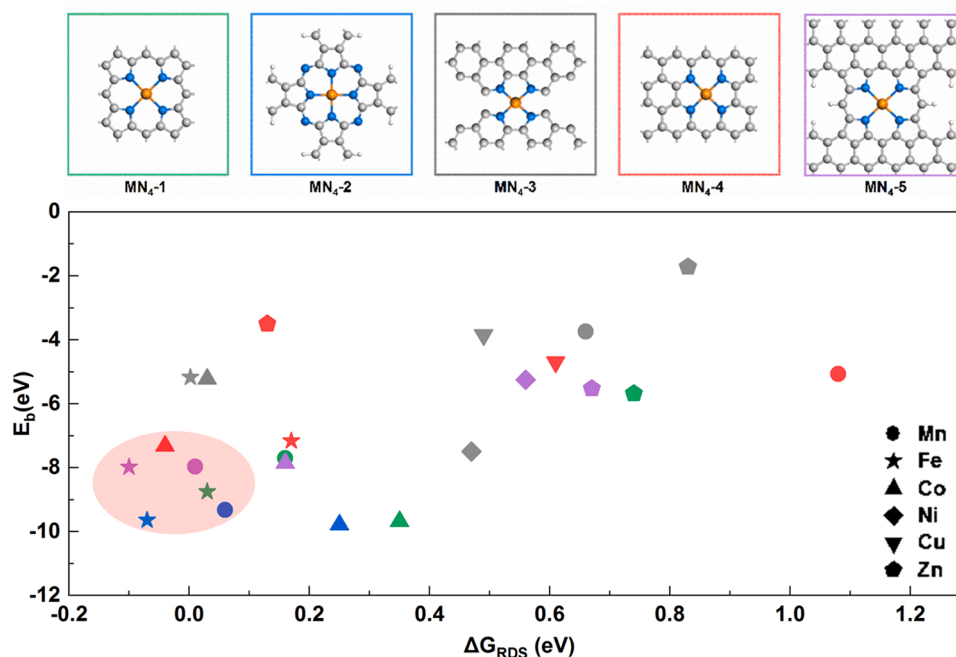
**Fig. 6.** The activity and stability mapping of active site by using binding energy as the stability descriptor and energy barrier of RDS as the activity descriptor (green: porphyrin-like $MN_4$, blue: phthalocyanine-like $MN_4$, gray: $MN_4C_8$, red: $MN_4C_{10}$, purple: $MN_4C_{12}$ M= Mn, Fe, Co, Ni, Cu, Zn).

making them easier to form in the unruly pyrolysis (Fig. S26 and Table S11), thus is expected to become the promising candidates [56–58]. Moreover, though a rapid degradation is generally observed, the stable running of PEMFCs based on Fe-N-C for hundreds of hours has ever been achieved at a relatively low potential (~0.4 V) [9,59]. That may be due to the weaker adsorption of oxygenated intermediate and lower electric field intensity according to this work. Therefore, the optimization of operating point is also an effective pathway.

## 4. Conclusion

In summary, we have demonstrated that Fe demetallation is responsible for the degradation of Fe-N-C and the influence of structure and structural evolution of active site is investigated. As revealed by EoT and in-situ Mössbauer spectroscopy, D1 is determined as the active site of ORR but suffers the most severe demetallation; D2 is relatively stable but contributes less to ORR at low overpotential. By bridging DFT calculations, both $FeN_4C_8$ and $FeN_4C_{12}$ assigned to D1 exhibit high ORR activity, and $FeN_4C_{10}$ assigned to D2 is less active. But the strength of Fe-N coordination in these sites is distinct with an order of $FeN_4C_{12}$ > $FeN_4C_{10}$ > $FeN_4C_8$. Therefore, the fast degradation at the early stage can be attributed to the demetallation of $FeN_4C_8$, while the more stable $FeN_4C_{12}$ contributes to the subsequent activity. During ORR, the structural evolution induced the oxygenated intermediate and electric field leads to the longer and more fragile Fe-N bond in $FeN_4$ sites. The stronger adsorption of oxygenated intermediate and the more violet vibration results in the faster demetallation at higher potential. On this basis, some promising structures with robust coordination are explore to improve the stability. The optimization of the operating voltage is also suggested. This exploratory work provides the insight into the mechanism of demetallation at the molecular level and the directional guidance for the future development of stable NPMCs in fuel cell devices.

## CRediT authorship contribution statement

**Xinlong Xu**: Investigation, Conceptualization, Methodology, Funding acquisition, Data curation, Formal analysis, Writing – original draft. **Xiaoming Zhang**: Investigation, Methodology. **Zhichong Kuang**:

Methodology. **Zhangxun Xia**: Formal analysis. **Alexandre I. Rykov**: Formal analysis. **Shansheng Yu**: Resources. **Junhu Wang**: Resources, Supervision. **Suli Wang**: Conceptualization, Supervision, Writing – review & editing. **Gongquan Sun**: Conceptualization, Supervision.

## Declaration of Competing Interest

The authors declare that they have no known competing financial interests or personal relationships that could have appeared to influence the work reported in this paper.

## Appendix A. Supporting information

Supplementary data associated with this article can be found in the online version at doi:10.1016/j.apcatb.2022.121290.

## References

[1] B.C. Steele, A. Heinzel, Materials for fuel-cell technologies, Nature 414 (2001) 345–352, https://doi.org/10.1038/35104620.

[2] F.T. Wagner, B. Lakshmanan, M.F. Mathias, Electrochemistry and the future of the automobile, J. Phys. Chem. Lett. 1 (2010) 2204–2219, https://doi.org/10.1021/jz100553m.

[3] M.K. Debe, Electrocatalyst approaches and challenges for automotive fuel cells, Nature 486 (2012) 43–51, https://doi.org/10.1038/nature11115.

[4] K. Gong, F. Du, Z. Xia, M. Durstock, L. Dai, Nitrogen-doped carbon nanotube arrays with high electrocatalytic activity for oxygen reduction, Science 323 (2009) 760–764, https://doi.org/10.1126/science.1168049.

[5] J. Suntivich, H.A. Gasteiger, N. Yabuuchi, H. Nakanishi, J.B. Goodenough, Y. Shao-Horn, Design principles for oxygen-reduction activity on perovskite oxide catalysts for fuel cells and metal-air batteries, Nat. Chem. 3 (2011) 546–550, https://doi.org/10.1038/nchem.1069.

[6] M. Sun, D. Davenport, H. Liu, J. Qu, M. Elimelech, J. Li, Highly efficient and sustainable non-precious-metal Fe–N–C electrocatalysts for the oxygen reduction

reaction, J. Mater. Chem. A 6 (2018) 2527–2539, https://doi.org/10.1039/c7ta09187g.

[7] X. Wan, X. Liu, Y. Li, R. Yu, L. Zheng, W. Yan, H. Wang, M. Xu, J. Shui, Fe–N–C electrocatalyst with dense active sites and efficient mass transport for high-performance proton exchange membrane fuel cells, Nat. Catal. 2 (2019) 259–268, https://doi.org/10.1038/s41929-019-0237-3.

[8] H. Zhang, H.T. Chung, D.A. Cullen, S. Wagner, U.I. Kramm, K.L. More, P. Zelenay, G. Wu, High-performance fuel cell cathodes exclusively containing atomically dispersed iron active sites, Energy Environ. Sci. 12 (2019) 2548–2558, https://doi.org/10.1039/c9ee00877b.

[9] M. Ferrandon, X. Wang, A.J. Kropf, D.J. Myers, G. Wu, C.M. Johnston, P. Zelenay, Stability of iron species in heat-treated polyaniline–iron–carbon polymer electrolyte fuel cell cathode catalysts, Electrochim. Acta 110 (2013) 282–291, https://doi.org/10.1016/j.electacta.2013.03.183.

[10] G. Wu, K.L. More, C.M. Johnston, P. Zelenay, High-performance electrocatalysts for oxygen reduction derived from polyaniline, iron, and cobalt, Science 332 (2011) 443–447, https://doi.org/10.1126/science.1200832.

[11] U. Martinez, S. Komini Babu, E.F. Holby, P. Zelenay, Durability challenges and perspective in the development of PGM-free electrocatalysts for the oxygen reduction reaction, Curr. Opin. Electrochem. 9 (2018) 224–232, https://doi.org/10.1016/j.coelec.2018.04.010.

[12] K. Kumar, L. Dubau, M. Mermoux, J. Li, A. Zitolo, J. Nelayah, F. Jaouen, F. Maillard, On the influence of oxygen on the degradation of Fe-N-C catalysts, Angew. Chem. Int. Ed. Engl. 59 (2020) 3235–3243, https://doi.org/10.1002/anie.201912451.

[13] C.H. Choi, H.-K. Lim, M.W. Chung, G. Chon, N. Ranjbar Sahraie, A. Altin, M.-T. Sougrati, L. Stievano, H.S. Oh, E.S. Park, F. Luo, P. Strasser, G. Dražić, K.J. J. Mayrhofer, H. Kim, F. Jaouen, The Achilles' heel of iron-based catalysts during oxygen reduction in an acidic medium, Energy Environ. Sci. 11 (2018) 3176–3182, https://doi.org/10.1039/c8ee01855c.

[14] J. Li, M.T. Sougrati, A. Zitolo, J.M. Ablett, I.C. Oğuz, T. Mineva, I. Matanovic, P. Atanassov, Y. Huang, I. Zenyuk, A. Di Cicco, K. Kumar, L. Dubau, F. Maillard, G. Dražić, F. Jaouen, Identification of durable and non-durable FeNx sites in Fe–N–C materials for proton exchange membrane fuel cells, Nat. Catal. (2020), https://doi.org/10.1038/s41929-020-00545-2.

[15] L.M. Roen, C.H. Paik, T.D. Jarvic, Electrocatalytic corrosion of carbon support in PEMFC cathodes, Electrochem. Solid State 7 (2004) A19–A22, https://doi.org/10.1149/1.1630412.

[16] G. Zhang, R. Chenitz, M. Lefèvre, S. Sun, J.-P. Dodelet, Is iron involved in the lack of stability of Fe/N/C electrocatalysts used to reduce oxygen at the cathode of PEM fuel cells? Nano Energy 29 (2016) 111–125, https://doi.org/10.1016/j.nanoen.2016.02.038.

[17] H. Zhang, S. Hwang, M. Wang, Z. Feng, S. Karakalos, L. Luo, Z. Qiao, X. Xie, C. Wang, D. Su, Y. Shao, G. Wu, Single atomic iron catalysts for oxygen reduction in acidic media: particle size control and thermal activation, J. Am. Chem. Soc. 139 (2017) 14143–14149, https://doi.org/10.1021/jacs.7b06514.

[18] A. Zitolo, V. Goellner, V. Armel, M.T. Sougrati, T. Mineva, L. Stievano, E. Fonda, F. Jaouen, Identification of catalytic sites for oxygen reduction in iron- and nitrogen-doped graphene materials, Nat. Mater. 14 (2015) 937–942, https://doi.org/10.1038/nmat4367.

[19] H.T. Chung, D.A. Cullen, D. Higgins, B.T. Sneed, E.F. Holby, K.L. More, P. Zelenay, Direct atomic-level insight into the active sites of a high-performance PGM-free ORR catalyst, Science 357 (2017) 479–484, https://doi.org/10.1126/science.aan2255.

[20] C.H. Choi, C. Baldizzone, G. Polymeros, E. Pizzutilo, O. Kasian, A.K. Schuppert, N. Ranjbar Sahraie, M.-T. Sougrati, K.J.J. Mayrhofer, F. Jaouen, Minimizing operando demetallation of Fe-N-C electrocatalysts in acidic medium, ACS Catal. 6 (2016) 3136–3146, https://doi.org/10.1021/acscatal.6b00643.

[21] Y. Nabae, Q. Yuan, S. Nagata, K. Kusaba, T. Aoki, N. Takao, T. Itoh, M. Arao, H. Imai, K. Higashi, T. Sakata, T. Uruga, Y. Iwasawa, In situ X-ray absorption spectroscopy to monitor the degradation of Fe/N/C cathode catalyst in proton exchange membrane fuel cells, J. Electrochem. Soc. 168 (2021), https://doi.org/10.1149/1945-7111/abdc64.

[22] E.F. Holby, G. Wang, P. Zelenay, Acid stability and demetalation of PGM-free ORR electrocatalyst structures from density functional theory: a model for "single-atom catalyst" dissolution, ACS Catal. (2020) 14527–14539, https://doi.org/10.1021/acscatal.0c02856.

[23] Z. Chen, S. Jiang, G. Kang, D. Nguyen, G.C. Schatz, R.P. Van Duyne, Operando characterization of iron phthalocyanine deactivation during oxygen reduction reaction using electrochemical tip-enhanced Raman spectroscopy, J. Am. Chem. Soc. 141 (2019) 15684–15692, https://doi.org/10.1021/jacs.9b07979.

[24] X. Zhang, Z. Xia, H. Li, S. Yu, S. Wang, G. Sun, Theoretical study of the strain effect on the oxygen reduction reaction activity and stability of FeNC catalyst, New J. Chem. 44 (2020) 6818–6824, https://doi.org/10.1039/c9nj06028f.

[25] I. Martinaiou, A. Shahraei, F. Grimm, H. Zhang, C. Wittich, S. Klemenz, S. J. Dolique, H.-J. Kleebe, R.W. Stark, U.I. Kramm, Effect of metal species on the stability of Me-N-C catalysts during accelerated stress tests mimicking the start-up and shut-down conditions, Electrochim. Acta 243 (2017) 183–196, https://doi.org/10.1016/j.electacta.2017.04.134.

[26] Y. Gao, M. Hou, M. Qi, L. He, H. Chen, W. Luo, Z. Shao, New insight into effect of potential on degradation of Fe-N-C catalyst for ORR, Front. Energy (2021), https://doi.org/10.1007/s11708-021-0727-2.

[27] P.G. Santori, F.D. Speck, J. Li, A. Zitolo, Q. Jia, S. Mukerjee, S. Cherevko, F. Jaouen, Effect of pyrolysis atmosphere and electrolyte pH on the oxygen reduction activity, stability and spectroscopic signature of FeNx moieties in Fe-N-C

[28] V. Goellner, C. Baldizzone, A. Schuppert, M.T. Sougrati, K. Mayrhofer, F. Jaouen, Degradation of Fe/N/C catalysts upon high polarization in acid medium, Phys. Chem. Chem. Phys. 16 (2014) 18454–18462, https://doi.org/10.1039/c4cp02882a.

[29] J. Li, S. Ghoshal, W. Liang, M.-T. Sougrati, F. Jaouen, B. Halevi, S. McKinney, G. McCool, C. Ma, X. Yuan, Z.-F. Ma, S. Mukerjee, Q. Jia, Structural and mechanistic basis for the high activity of Fe–N–C catalysts toward oxygen reduction, Energy Environ. Sci. 9 (2016) 2418–2432, https://doi.org/10.1039/c6ee01160h.

[30] L. Osmieri, R.K. Ahluwalia, X. Wang, H.T. Chung, X. Yin, A.J. Kropf, J. Park, D. A. Cullen, K.L. More, P. Zelenay, D.J. Myers, K.C. Neyerlin, Elucidation of Fe-N-C electrocatalyst active site functionality via in-situ X-ray absorption and operando determination of oxygen reduction reaction kinetics in a PEFC, Appl. Catal. B Environ. 257 (2019), https://doi.org/10.1016/j.apcatb.2019.117929.

[31] B. Delley, An all-electron numerical-method for solving the local density functional for polyatomic-molecules, J. Chem. Phys. 92 (1990) 508–517, https://doi.org/10.1063/1.458452.

[32] B. Delley, From molecules to solids with the DMol(3) approach, J. Chem. Phys. 113 (2000) 7756–7764, https://doi.org/10.1063/1.1316015.

[33] X. Xu, X. Zhang, Z. Xia, R. Sun, H. Li, J. Wang, S. Yu, S. Wang, G. Sun, Solid phase microwave-assisted fabrication of Fe-doped ZIF-8 for single-atom Fe-N-C electrocatalysts on oxygen reduction, J. Energy Chem. 54 (2021) 579–586, https://doi.org/10.1016/j.jechem.2020.06.046.

[34] H. Wang, W. An, X. Liu, C. Heath Turner, Oxygen reduction reaction on Pt(1 1 1), Pt(2 2 1), and Ni/Au1Pt3(2 2 1) surfaces: probing scaling relationships of reaction energetics and interfacial composition, Chem. Eng. Sci. 184 (2018) 239–250, https://doi.org/10.1016/j.ces.2018.03.054.

[35] D. Zhao, J.L. Shui, L.R. Grabstanowicz, C. Chen, S.M. Commet, T. Xu, J. Lu, D. J. Liu, Highly efficient non-precious metal electrocatalysts prepared from one-pot synthesized zeolitic imidazolate frameworks, Adv. Mater. 26 (2014) 1093–1097, https://doi.org/10.1002/adma.201304238.

[36] Y.-H. Lee, K.-H. Chang, C.-C. Hu, Differentiate the pseudocapacitance and double-layer capacitance contributions for nitrogen-doped reduced graphene oxide in acidic and alkaline electrolytes, J. Power Sources 227 (2013) 300–308, https://doi.org/10.1016/j.jpowsour.2012.11.026.

[37] T. Lin, I.W. Chen, F. Liu, C. Yang, H. Bi, F. Xu, F. Huang, Nitrogen-doped mesoporous carbon of extraordinary capacitance for electrochemical energy storage, Science 350 (2015) 1508–1513, https://doi.org/10.1126/science.aab3798.

[38] G. Liu, X. Li, J.-W. Lee, B.N. Popov, A review of the development of nitrogen-modified carbon-based catalysts for oxygen reduction at USC, Catal. Sci. Technol. 1 (2011), https://doi.org/10.1039/c0cy00053a.

[39] J. Li, S. Chen, N. Yang, M. Deng, S. Ibraheem, J. Deng, J. Li, L. Li, Z. Wei, Ultrahigh-loading zinc single-atom catalyst for highly efficient oxygen reduction in both acidic and alkaline media, Angew. Chem. Int. Ed. Engl. 58 (2019) 7035–7039, https://doi.org/10.1002/anie.201902109.

[40] W. Wang, Q. Jia, S. Mukerjee, S. Chen, Recent insights into the oxygen-reduction electrocatalysis of Fe/N/C materials, ACS Catal. 9 (2019) 10126–10141, https://doi.org/10.1021/acscatal.9b02583.

[41] X. Zhang, Q. Liu, J. Shui, Effect of catalyst layer hydrophobicity on Fe−N−C proton exchange membrane fuel cells, ChemElectroChem 7 (2020) 1775–1780, https://doi.org/10.1002/celc.202000351.

[42] J. Chen, X. Yan, C. Fu, Y. Feng, C. Lin, X. Li, S. Shen, C. Ke, J. Zhang, Insight into the rapid degradation behavior of nonprecious metal Fe-N-C electrocatalyst-based proton exchange membrane fuel cells, ACS Appl. Mater. Interfaces 11 (2019) 37779–37786, https://doi.org/10.1021/acsami.9b13474.

[43] U.I. Kramm, L. Ni, S. Wagner, (57) Fe Mossbauer spectroscopy characterization of electrocatalysts, Adv. Mater. (2019), e1805623, https://doi.org/10.1002/adma.201805623.

[44] C.A. Melendres, Mossbauer and Raman-spectra of carbon-supported iron phthalocyanine, J. Phys. Chem. 84 (1980) 1936–1939, https://doi.org/10.1021/j100452a014.

[45] J.L. Kneebone, S.L. Daifuku, J.A. Kehl, G. Wu, H.T. Chung, M.Y. Hu, E.E. Alp, K. L. More, P. Zelenay, E.F. Holby, M.L. Neidig, A Combined probe-molecule, Mössbauer, nuclear resonance vibrational spectroscopy, and density functional theory approach for evaluation of potential iron active sites in an oxygen reduction reaction catalyst, J. Phys. Chem. C 121 (2017) 16283–16290, https://doi.org/10.1021/acs.jpcc.7b03779.

[46] T. Mineva, I. Matanovic, P. Atanassov, M.-T. Sougrati, L. Stievano, M. Clémancey, A. Kochem, J.-M. Latour, F. Jaouen, Understanding active sites in pyrolyzed Fe–N–C catalysts for fuel cell cathodes by bridging density functional theory calculations and 57Fe Mössbauer spectroscopy, ACS Catal. 9 (2019) 9359–9371, https://doi.org/10.1021/acscatal.9b02586.

[47] U.I. Kramm, J. Herranz, N. Larouche, T.M. Arruda, M. Lefevre, F. Jaouen, P. Bogdanoff, S. Fiechter, I. Abs-Wurmbach, S. Mukerjee, J.P. Dodelet, Structure of the catalytic sites in Fe/N/C-catalysts for O2-reduction in PEM fuel cells, Phys. Chem. Chem. Phys. 14 (2012) 11673–11688, https://doi.org/10.1039/c2cp41957b.

[48] N.R. Sahraie, U.I. Kramm, J. Steinberg, Y. Zhang, A. Thomas, T. Reier, J. P. Paraknowitsch, P. Strasser, Quantifying the density and utilization of active sites in non-precious metal oxygen electroreduction catalysts, Nat. Commun. 6 (2015) 8618, https://doi.org/10.1038/ncomms9618.

[49] Q. Jia, N. Ramaswamy, H. Hafiz, U. Tylus, K. Strickland, G. Wu, B. Barbiellini, A. Bansil, E.F. Holby, P. Zelenay, S. Mukerjee, Experimental observation of redox-

induced Fe-N switching behavior as a determinant role for oxygen reduction activity, ACS Nano 9 (2015) 12496–12505, https://doi.org/10.1021/acsnano.5b05984.

[50] Y.Y. Jiang, P.J. Ni, C.X. Chen, Y.Z. Lu, P. Yang, B. Kong, A. Fisher, X. Wang, Selective electrochemical H2O2 production through two-electron oxygen electrochemistry, Adv. Energy Mater. 8 (2018), https://doi.org/10.1002/aenm.201801909.

[51] M. Xiao, J. Zhu, L. Ma, Z. Jin, J. Ge, X. Deng, Y. Hou, Q. He, J. Li, Q. Jia, S. Mukerjee, R. Yang, Z. Jiang, D. Su, C. Liu, W. Xing, Microporous framework induced synthesis of single-atom dispersed Fe-N-C acidic ORR catalyst and its in situ reduced Fe-N4 active site identification revealed by X-ray absorption spectroscopy, ACS Catal. (2018) 2824–2832, https://doi.org/10.1021/acscatal.8b00138.

[52] R. Chenitz, U.I. Kramm, M. Lefèvre, V. Glibin, G. Zhang, S. Sun, J.-P. Dodelet, A specific demetalation of Fe–N4 catalytic sites in the micropores of NC_Ar + NH3 is at the origin of the initial activity loss of the highly active Fe/N/C catalyst used for the reduction of oxygen in PEM fuel cells, Energy Environ. Sci. (2018), https://doi.org/10.1039/c7ee02302b.

[53] G.S. Karlberg, J. Rossmeisl, J.K. Norskov, Estimations of electric field effects on the oxygen reduction reaction based on the density functional theory, Phys. Chem. Chem. Phys. 9 (2007) 5158–5161, https://doi.org/10.1039/b705938h.

[54] K.Y. Yeh, M.J. Janik, Density functional theory-based electrochemical models for the oxygen reduction reaction: comparison of modeling approaches for electric field and solvent effects, J. Comput. Chem. 32 (2011) 3399–3408, https://doi.org/10.1002/jcc.21919.

[55] I.D. Brown, R.D. Shannon, Empirical bond-strength–bond-length curves for oxides, Acta Cryst. 29 (1973) 266–282, https://doi.org/10.1107/s0567739473000689.

[56] J. Li, M. Chen, D.A. Cullen, S. Hwang, M. Wang, B. Li, K. Liu, S. Karakalos, M. Lucero, H. Zhang, C. Lei, H. Xu, G.E. Sterbinsky, Z. Feng, D. Su, K.L. More, G. Wang, Z. Wang, G. Wu, Atomically dispersed manganese catalysts for oxygen reduction in proton-exchange membrane fuel cells, Nat. Catal. (2018), https://doi.org/10.1038/s41929-018-0164-8.

[57] X. Xie, C. He, B. Li, Y. He, D.A. Cullen, E.C. Wegener, A.J. Kropf, U. Martinez, Y. Cheng, M.H. Engelhard, M.E. Bowden, M. Song, T. Lemmon, X.S. Li, Z. Nie, J. Liu, D.J. Myers, P. Zelenay, G. Wang, G. Wu, V. Ramani, Y. Shao, Performance enhancement and degradation mechanism identification of a single-atom Co–N–C catalyst for proton exchange membrane fuel cells, Nat. Catal. 3 (2020) 1044–1054, https://doi.org/10.1038/s41929-020-00546-1.

[58] Y. He, S. Hwang, D.A. Cullen, M.A. Uddin, L. Langhorst, B. Li, S. Karakalos, A. J. Kropf, E.C. Wegener, J. Sokolowski, M. Chen, D. Myers, D. Su, K.L. More, G. Wang, S. Litster, G. Wu, Highly active atomically dispersed CoN4 fuel cell cathode catalysts derived from surfactant-assisted MOFs: carbon-shell confinement strategy, Energy Environ. Sci. 12 (2019) 250–260, https://doi.org/10.1039/c8ee02694g.

[59] Y.-C. Wang, L. Huang, P. Zhang, Y.-T. Qiu, T. Sheng, Z.-Y. Zhou, G. Wang, J.-G. Liu, M. Rauf, Z.-Q. Gu, W.-T. Wu, S.-G. Sun, Constructing a triple-phase interface in micropores to boost performance of Fe/N/C catalysts for direct methanol fuel cells, ACS Energy Lett. 2 (2017) 645–650, https://doi.org/10.1021/acsenergylett.7b00071.